



Tropopause Evolution in a Rapidly Intensifying Tropical Cyclone: A Static Stability Budget Analysis in an Idealized Axisymmetric Framework

PATRICK DURAN^a AND JOHN MOLINARI

University at Albany, State University of New York, Albany, New York

(Manuscript received 26 March 2018, in final form 5 November 2018)

ABSTRACT

Upper-level static stability (N^2) variations can influence the evolution of the transverse circulation and potential vorticity in intensifying tropical cyclones (TCs). This paper examines these variations during the rapid intensification (RI) of a simulated TC. Over the eye, N^2 near the tropopause decreases and the cold-point tropopause rises by up to 4 km at the storm center. Outside of the eye, N^2 increases considerably just above the cold-point tropopause and the tropopause remains near its initial level. A budget analysis reveals that the advection terms, which include differential advection of potential temperature θ and direct advection of N^2 , are important throughout the upper troposphere and lower stratosphere. These terms are particularly pronounced within the eye, where they destabilize the layer near and above the cold-point tropopause. Outside of the eye, a radial–vertical circulation develops during RI, with strong outflow below the tropopause and weak inflow above. Differential advection of θ near the outflow jet provides forcing for stabilization below the outflow maximum and destabilization above. Turbulence induced by vertical wind shear on the flanks of the outflow maximum also modifies the vertical stability profile. Meanwhile, radiative cooling tendencies at the top of the cirrus canopy generally act to destabilize the upper troposphere and stabilize the lower stratosphere. The results suggest that turbulence and radiation, alongside differential advection, play fundamental roles in the upper-level N^2 evolution of TCs. These N^2 tendencies could have implications for both the TC diurnal cycle and the tropopause-layer potential vorticity evolution in TCs.

1. Introduction

Using a high-resolution dropsonde dataset collected during the Tropical Cyclone Intensity Experiment (TCI; Doyle et al. 2017), Duran and Molinari (2018) observed dramatic changes in tropopause structure during the rapid intensification (RI) of Hurricane Patricia (2015). The goal of the present paper is to analyze the processes that might have produced the upper-tropospheric and lower-stratospheric fluctuations observed in Patricia, using an idealized axisymmetric simulation.

After undergoing a remarkably rapid intensification, Hurricane Patricia (2015) attained the strongest wind speed ever recorded in a tropical cyclone (TC; Kimberlain et al. 2016; Rogers et al. 2017). TCI dropsonde observations collected during this RI period revealed dramatic changes in the cold-point tropopause height and upper-level static stability (Duran and Molinari 2018). In

particular, when Patricia was at tropical storm intensity shortly before RI commenced, a strong inversion layer existed just above the cold-point tropopause (see their Fig. 4a). During the first half of the RI period, this inversion layer weakened throughout Patricia's inner core, with the weakening most pronounced over the developing eye. By the time the storm reached its maximum best-track intensity of 95 m s^{-1} , the inversion layer over the eye had disappeared almost completely (see their Fig. 4d), which was accompanied by a greater than 1-km increase in the tropopause height. Meanwhile outside of the eye, the static stability remained large and the tropopause stayed near its initial level.

Despite the importance of tropopause-layer thermodynamics in theoretical models of hurricanes (Emanuel and Rotunno 2011; Emanuel 2012), most observational studies of the upper-tropospheric structure of TCs are decades old.¹ Recently, however, Komaromi and Doyle (2017) found that stronger TCs tended to have a higher

^a Current affiliation: Earth System Science Center, University of Alabama in Huntsville, Huntsville, Alabama.

Corresponding author: Patrick Duran, patrick.duran@uah.edu

¹ An in-depth review of these papers can be found in Duran and Molinari (2018).

and warmer tropopause over their inner core than weaker TCs. Their results are consistent with the evolution observed over the inner core of Hurricane Patricia, in which the tropopause height increased and the tropopause temperature warmed throughout RI (Duran and Molinari 2018).

An idealized simulation of a TC analyzed by Ohno and Satoh (2015) suggested that the development of an upper-level warm core near the 13-km level acted to decrease the static stability near the tropopause within the eye. During the early stage of development in their simulation, large static stability existed above 16 km at all radii (their Fig. 9c). After the storm's intensification, however, the static stability within the eye above 16 km was markedly smaller (their Fig. 10c). Although the mechanisms that might drive this static stability evolution have not been examined explicitly, it might be related to the development of an upper-tropospheric warm core within the eye.

Stern and Zhang (2013) described the development of the TC warm core in a three-dimensional framework using a potential temperature (θ) budget analysis. Although the warm anomaly in their simulation maximized in the midlevels, they noted that a secondary warming maximum also existed in the 12–14-km layer. In the midlevels, both radial and vertical advection played important roles in the development of the warm core, with the eddy component of radial advection dominating over the mean component. In the upper levels, however, only the mean component of vertical advection considerably affected warm-core development. Horizontal diffusion became particularly large near the outer edge of the eye during the later stage of RI; these diffusive tendencies produced regions of warming below regions of cooling (Stern and Zhang 2013, their Fig. 7t) that would act to decrease the vertical θ gradient. Potential temperature tendencies associated with these advective and diffusive processes could contribute to a decrease in static stability near the tropopause within the eye.

Outside of the eye, in the presence of cirrus clouds, vertical gradients of radiative heating also can modify the tropopause-layer static stability. Bu et al. (2014) noted the existence of a shallow region of diurnal-mean net radiative cooling at the top of the TC cirrus canopy (see their Figs. 5 and 11). This shallow region of cooling could act to destabilize the layer just below the top of the cirrus canopy and to stabilize the layer immediately above. If the top of the cirrus canopy lies close to the tropopause, then these radiative processes could contribute to a stabilization of the lower stratosphere.

In addition to the direct effect of radiative cooling on the tropopause-layer static stability, this cooling also

could exert an indirect effect by modifying the storm's radial–vertical circulation. Although cloud-top cooling played a negligible role in the radiatively induced storm expansion observed by Bu et al. (2014) and Fovell et al. (2016), it did modify the circulation near the cloud top. In particular, it drove weak inflow above the cooling maximum and outflow below, along with subsidence within the region of cooling (Fovell et al. 2016, their Fig. 21). Conversely, Durran et al. (2009) described the circulation that developed in response to radiative heating within tropopause-layer cirrus clouds. This heating induced upward motion through the heat source, inflow below the heat source, and outflow above. Dinh et al. (2010) showed that these circulations act to spread cirrus clouds laterally, which then would feed back onto the radiative tendencies. Although these circulations were weak, their persistence could drive differential advection of θ , as discussed by Chen and Zhang (2013) and Chen and Gopalakrishnan (2015), which would modify the tropopause-layer static stability.

The existence of a diurnal cycle of TC convection has been well established in recent literature (e.g., Kossin 2002; Dunion et al. 2014; Bowman and Fowler 2015; Leppert and Cecil 2016). Since this cycle exhibits a convective maximum overnight and in the early morning, and a convective minimum in the afternoon, radiative heating tendencies are a natural suspect in its evolution. The idealized simulations of Navarro and Hakim (2016) implicate periodic oscillations of upper-level radiative heating in the evolution of the TC diurnal cycle. Their results exhibit characteristics of an inertia–gravity wave response with an outward-propagating horizontal phase speed of 9.8 m s^{-1} , which is consistent with the outward motion of the diurnal pulse observed by Dunion et al. (2014). If the diurnal pulse is, indeed, an outward-propagating inertia–gravity wave, then the upper-tropospheric static stability profile could have implications for the characteristics of its propagation.

To our knowledge, the only paper that has examined explicitly the static stability evolution in a modeled TC is Kepert et al. (2016), but their analysis was limited to the boundary layer. The analysis herein is based upon that of Stern and Zhang (2013), except using a static stability budget similar to that of Kepert et al. (2016), with a focus on the upper-tropospheric and lower-stratospheric evolution during RI.

2. Model setup

The numerical simulations were performed using version 19.4 of Cloud Model 1 (CM1) described in Bryan and Rotunno (2009). The equations of motion were integrated on a 3000-km-wide, 30-km-deep axisymmetric

grid with uniform 1-km horizontal and 250-m vertical grid spacing. The computations were performed on an f plane at 15°N latitude, over a sea surface with a constant temperature of 30.5°C, which is based on that analyzed near Hurricane Patricia (2015; Kimberlain et al. 2016). Horizontal turbulence was parameterized using the Smagorinsky scheme described in Bryan and Rotunno (2009, p. 1773), with a prescribed mixing length that varied linearly from 100 m at a surface pressure of 1015 hPa to 1000 m at a surface pressure of 900 hPa. Vertical turbulence was parameterized using the formulation of Markowski and Bryan [2016, their Eq. (6)], using an asymptotic vertical mixing length of 100 m, which is the default setup for hurricane simulations in CM1. A Rayleigh damping layer was applied outside of the 2900-km radius and above the 25-km level to prevent spurious gravity wave reflection at the model boundaries. Microphysical processes were parameterized using the Thompson et al. (2004) scheme, and radiative heating tendencies were computed every 2 min using the Rapid Radiative Transfer Model for GCMs (RRTMG) longwave and shortwave schemes (Iacono et al. 2008). The initial environmental temperature and humidity field was horizontally homogeneous and determined by averaging all Climate Forecast System Reanalysis (CFSR) grid points within 100 km of Patricia’s center of circulation at 1800 UTC 21 October 2015. The balanced vortex described in Rotunno and Emanuel [1987, their Eq. (37)] was used to initialize the wind field, setting all parameters equal to the values used therein.

Since ocean coupling and asymmetric forcing are present in nature, the intent of this paper is not to formally simulate Hurricane Patricia. Rather, the intent is to simulate a storm with a similar intensification rate and to examine the processes that produced the stability variations in the simulated storm. After an initial spinup period of about 20 h, the modeled storm (Fig. 1, blue lines) began an RI period that lasted approximately 18 h. After this RI, the storm continued to intensify more slowly until the maximum 10-m wind speed reached 89 m s⁻¹, and the sea level pressure reached its minimum of 846 hPa, 81 h into the simulation. Hurricane Patricia (red asterisks) exhibited a similar intensity evolution prior to its landfall, with an RI period leading to a maximum 10-m wind speed of 95 m s⁻¹ and a minimum sea level pressure of 872 hPa.²

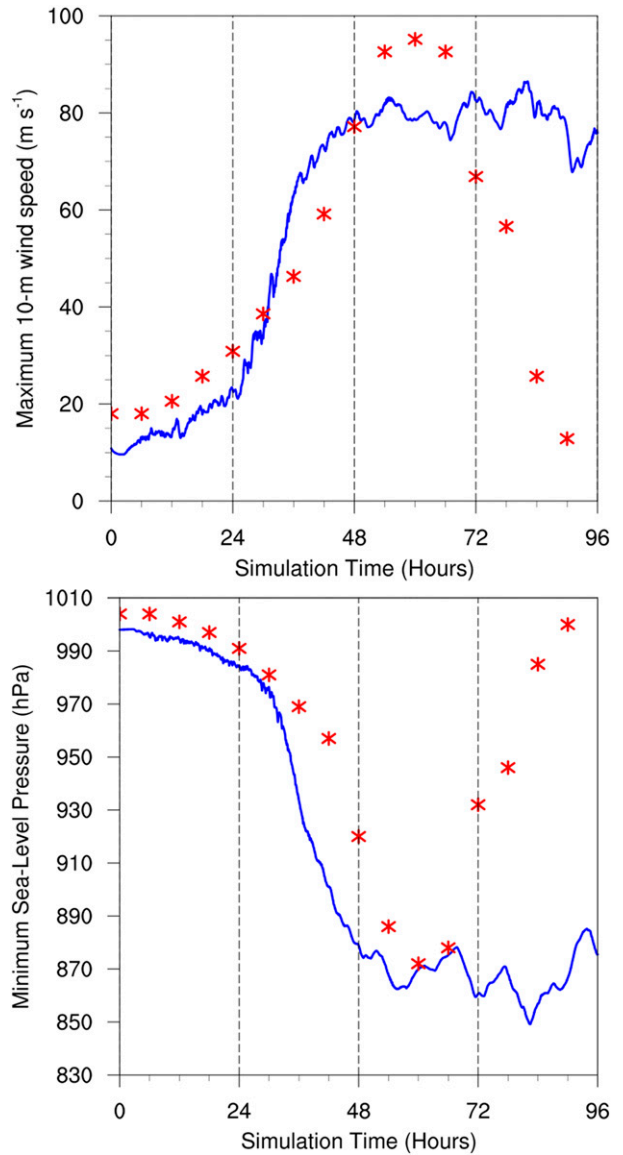


FIG. 1. (top) The maximum 10-m wind speed (m s⁻¹) and (bottom) minimum sea level pressure (hPa) in the simulated storm (blue lines; plotted every minute) and from Hurricane Patricia’s best track (red asterisks; plotted every 6 h beginning at the time Patricia attained tropical storm intensity). The rapid weakening during the later stage of Patricia’s lifetime was induced by landfall.

3. Budget computation

Following Bryan (2017), the static stability can be expressed as the squared Brunt–Väisälä frequency:

$$N_m^2 = \frac{g}{T} \left(\frac{\partial T}{\partial z} + \Gamma_m \right) \left(1 + \frac{T}{R_d/R_v + q_s} \frac{\partial q_s}{\partial T} \right) - \frac{g}{1 + q_t} \frac{\partial q_t}{\partial z}, \quad (1)$$

where g is gravitational acceleration; T is temperature; R_d and R_v are the gas constants of dry air and water

²Note that in Fig. 1, plotting of Patricia’s wind speed begins when it attained tropical storm strength at 0000 UTC 21 October 2015, rather than its first best-track entry. This was done to shift Patricia’s RI period in the plot so that it occurs near the same time as the modeled storm’s RI period.

vapor, respectively; q_s is the saturation mixing ratio; q_t is the total condensate mixing ratio; and Γ_m is the moist adiabatic lapse rate:

$$\Gamma_m = g(1 + q_t) \left(\frac{1 + L_v q_s / R_d T}{c_{pm} + L_v \partial q_s / \partial T} \right), \quad (2)$$

where L_v is the latent heat of vaporization and c_{pm} is the specific heat of moist air at constant pressure. In the tropopause layer, q_s , q_t , $\partial q_s / \partial T$, and $\partial q_t / \partial z$ approach zero. In this limiting case, Eq. (1) reduces to

$$N^2 = \frac{g}{\theta} \frac{\partial \theta}{\partial z}, \quad (3)$$

where θ is the potential temperature.

Equation (1) is the appropriate expression for N^2 in moist environments, whereas Eq. (3) applies strictly in the absence of moisture. Although the tropopause layer is not completely dry, moisture is small enough there for Eq. (3) to be a good approximation of N^2 in the budget computation.³

Taking the time derivative of Eq. (3) and switching the order of differentiation yields the static stability tendency:

$$\frac{\partial N^2}{\partial t} = \frac{g}{\theta} \frac{\partial}{\partial z} \frac{\partial \theta}{\partial t} - \frac{g}{\theta^2} \frac{\partial \theta}{\partial z} \frac{\partial \theta}{\partial t}, \quad (4)$$

where the potential temperature tendency $\partial \theta / \partial t$ can be written, following Bryan (2017):

$$\begin{aligned} \frac{\partial \theta}{\partial t} = & -u \frac{\partial \theta}{\partial r} - w \frac{\partial \theta}{\partial z} + \text{HTURB} + \text{VTURB} + \text{MP} \\ & + \text{RAD} + \text{DISS}. \end{aligned} \quad (5)$$

Each term on the right-hand side of Eq. (5) represents a θ budget variable, each of which is output directly by the model every minute.

The first term on the right-hand side of Eq. (4) is an order of magnitude larger than the second term throughout most of the tropopause layer (not shown).⁴ Consequently, the contribution of each of the terms in Eq. (5) to the N^2 tendency can be interpreted in terms of a vertical gradient of each term.

Taking the vertical gradient of the first two terms on the right-hand side of Eq. (5) yields the time tendency of the vertical θ gradient resulting from horizontal and vertical advection:

$$\left(\frac{\partial}{\partial t} \frac{\partial \theta}{\partial z} \right)_{\text{adv}} = -u \frac{\partial}{\partial r} \frac{\partial \theta}{\partial z} - w \frac{\partial}{\partial z} \frac{\partial \theta}{\partial z} - \frac{\partial u}{\partial z} \frac{\partial \theta}{\partial r} - \frac{\partial w}{\partial z} \frac{\partial \theta}{\partial z}. \quad (6)$$

The first two terms on the right-hand side of Eq. (6) represent advection of static stability by the radial and vertical wind, respectively. These terms act to rearrange the static stability field, but they cannot strengthen or weaken static stability maxima or minima. The third and fourth terms on the right-hand side of Eq. (6) represent, respectively, the tilting of isentropes in the presence of vertical wind shear and the stretching or squashing of isentropes by vertical gradients of vertical velocity. Since these terms involve velocity gradients, they can act to strengthen or weaken static stability maxima or minima through differential advection. Unless otherwise stated, any reference to ‘‘advection’’ in this paper indicates the sum of all of the terms in Eq. (6).

Returning to Eq. (5), HTURB and VTURB are the θ tendencies from the horizontal and vertical turbulence parameterizations, respectively; MP is the tendency from the microphysics scheme; RAD is the tendency from the radiation scheme; and DISS is the tendency resulting from turbulent dissipation. This equation neglects Rayleigh damping, since the entire analysis domain (0–200-km radius, 14–21-km height) lies outside of the regions where damping is applied. Each term in Eq. (5) is substituted for $\partial \theta / \partial t$ in Eq. (4), yielding the contribution of each budget term to the static stability tendency. These terms are summed, yielding an instantaneous ‘‘budget change’’ in N^2 every minute. The budget changes are then averaged over 24-h (1440 min) periods, multiplied by the length of the time period, and compared to the total model change in N^2 over that same time period, that is,

$$\Delta N^2_{\text{budget}} = \frac{\delta t}{1440} \sum_{t=t_0}^{1440} \frac{\partial N^2}{\partial t} \Big|_t, \quad (7)$$

$$\Delta N^2_{\text{model}} = N^2_{t_0+\delta t} - N^2_{t_0}, \quad (8)$$

$$\text{Residual} = \Delta N^2_{\text{model}} - \Delta N^2_{\text{budget}}, \quad (9)$$

where t_0 is an initial time and δt is 24 h.

Equations (7)–(9) are evaluated for three consecutive 24-h periods in Fig. 2. For this and all subsequent radial–vertical cross sections, a 1–2–1 smoother is applied once in the radial direction to eliminate $2\Delta r$ noise that appears in some of the raw model output and calculated fields. The left column of Fig. 2 depicts the model changes computed using Eq. (8) together with Eq. (1) in saturated environments. The center column depicts the budget changes computed using Eq. (7)

³ The validity of this approximation will be substantiated later in this section.

⁴ The magnitude of the second term is comparable to that of the first only in a radially confined region near $r = 0$ in the stratosphere.

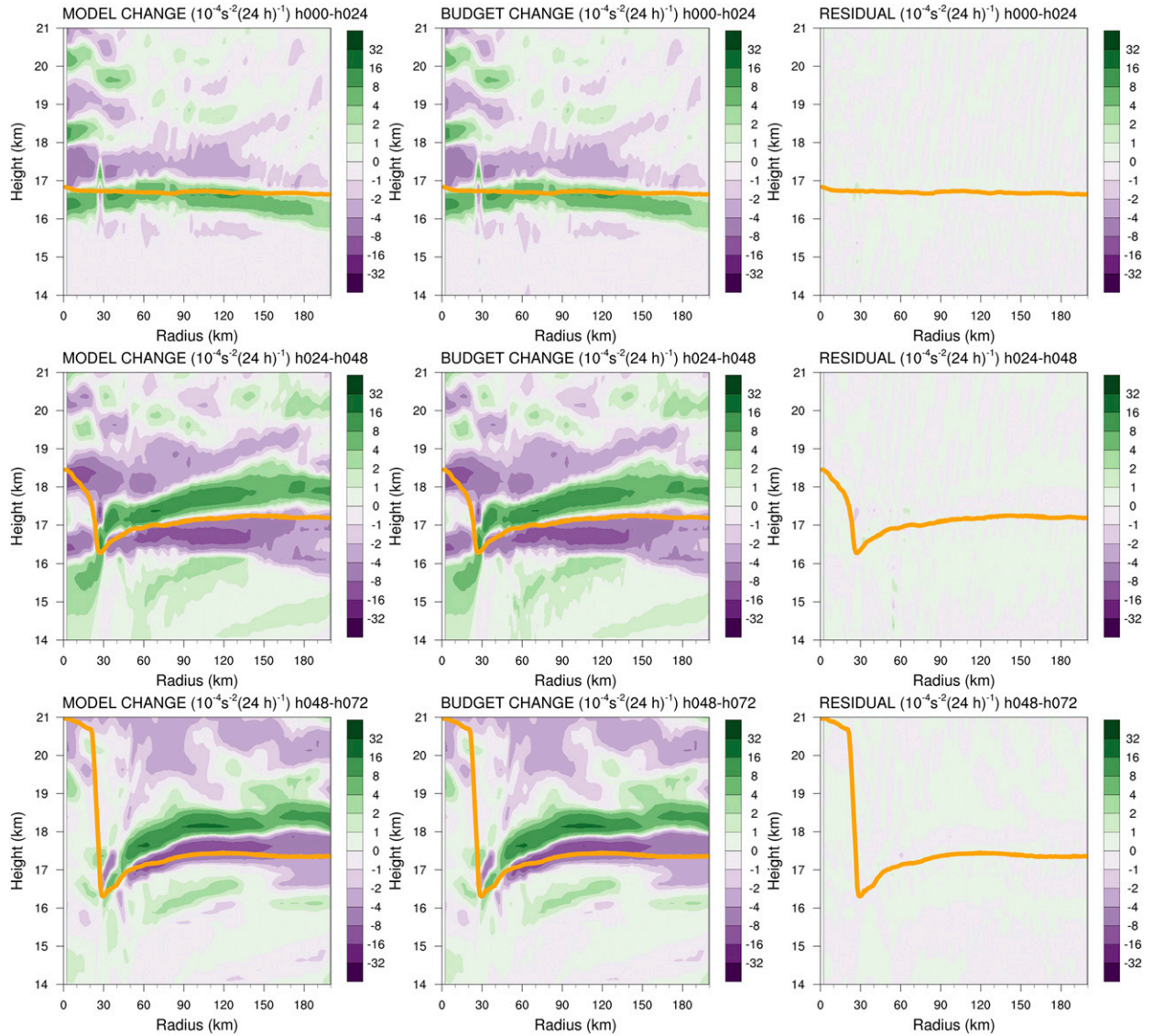


FIG. 2. (left) The 24-h changes in squared Brunt–Väisälä frequency N^2 (10^{-4} s^{-2}) computed using Eq. (8), together with Eq. (1), over (top) 0–24, (middle) 24–48, and (bottom) 48–72 h. (center) The N^2 change over the same time periods computed using Eqs. (3)–(7). (right) The budget residual over the same time periods, computed by subtracting the budget change in the center column from the model change in the left column. Orange lines represent the cold-point tropopause height averaged over the same time periods (i.e., the tropopause is determined every minute, and these tropopause heights are averaged over 24 h.)

together with Eq. (4) throughout the entire domain. Thus, the left column includes the effect of moisture in the N^2 computations, whereas the center column neglects moisture. The right column depicts the residuals, computed using Eq. (9) (i.e., the left column minus the center column.) In every 24-h period, the budget changes are nearly identical to the model changes, which is reflected in the near-zero residuals in the right column. This indicates that the budget accurately represents the model variability, which implies that the neglect of moisture in the budget

computation introduces negligible error within the analysis domain.⁵

In the tropopause layer, some of the budget terms are small enough to be ignored. To determine which of the terms are most important, a time series of the

⁵ This is not the case in the lower and midtroposphere, where the residual actually exceeds the budget tendencies in many places, likely resulting from the neglect of moisture; thus, we limit this analysis to the upper troposphere and lower stratosphere.

contribution of each of the budget terms in Eq. (5) to the tropopause-layer static stability tendency is plotted in Fig. 3. For this figure, each of the budget terms is computed using the method described in section 3, except with 1-h averaging intervals instead of 24-h intervals. The absolute values of these tendencies are then averaged over the radius–height domain of the plots shown in Fig. 2 and plotted as a time series.⁶ Advection (Fig. 3, red line) plays an essential role in the mean tropopause-layer static stability tendency at all times, and vertical turbulence (Fig. 3, blue line) and radiation (Fig. 3, dark green line) also contribute significantly. Variations in the magnitude and spatial structure of these terms drive the static stability changes depicted in Fig. 2; subsequent sections will focus on these variations and what causes them. The three remaining processes—horizontal turbulence, microphysics, and dissipative heating—are negligible everywhere outside of the eyewall and will not be included in the analysis.

4. Results

a. Static stability and tropopause evolution

The average N^2 over the first day of the simulation (Fig. 4a) indicates the presence of a weak N^2 maximum just above the cold-point tropopause. Over the subsequent 24 h, during the RI period, the N^2 maximum weakened within the 25-km radius (Fig. 4b). This decreasing N^2 corresponded to an increase in the tropopause height within the developing eye, maximized at the storm center. Just outside of the eye, meanwhile, the tropopause height decreased within the 25–60-km radial band and increased only slightly outside of the 60-km radius. Everywhere outside of the eye, the N^2 maximum just above the tropopause strengthened during RI. These trends continued as the storm's intensity leveled off in the 48–72-h period (Fig. 4c). The tropopause height increased to nearly 21 km at the storm center and sloped sharply downward to 16.3 km on the outer edge of the eye, near the 30-km radius. A local minimum in tropopause height manifested near the outer edge of the eye, similar to that observed in Hurricane Patricia (Duran and Molinari 2018, their Figs. 4f–h). The presence of a local minimum at this location in these 24-h averages suggests that this tropopause depression on the

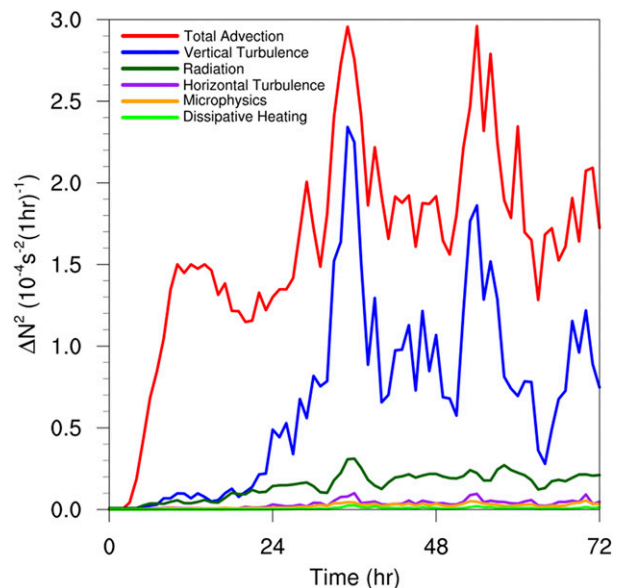


FIG. 3. Time series of the contribution of each of the budget terms to the time tendency of the squared Brunt–Väisälä frequency N^2 (10^{-4} s^{-2}). For each budget term, the absolute value of the N^2 tendency is averaged temporally over 1-h periods (using output every minute) and spatially in a region extending from 0- to 200-km radius and from 14- to 21-km altitude.

outer edge of the eye could be a robust, persistent feature. Static stability outside of the eye, meanwhile, continued to increase just above the cold-point tropopause. This N^2 evolution resembles that observed in Hurricane Patricia (2015; Duran and Molinari 2018, their Fig. 4). The mechanisms that led to these N^2 changes will be investigated in the subsequent sections.

b. Static stability budget analysis

1) 0–24 H

The initial spinup period was characterized by a steady increase of the maximum wind speed from 11 to 22 m s^{-1} (Fig. 1a, blue line). The weakening of the lower-stratospheric static stability maximum during this period is reflected in the total N^2 budget change over this time (Fig. 5a). The layer just above the cold-point tropopause was characterized by decreasing N^2 (purple shading), maximizing in magnitude at the storm center. At and immediately below the tropopause, meanwhile, N^2 increased during this time period (green shading). Although these tendencies extended out to the 200-km radius, they were particularly pronounced at the innermost radii. A comparison of the contributions of advection (Fig. 5b), vertical turbulence (Fig. 5c), and radiation (Fig. 5d) reveals that advection was the primary driver of the N^2 tendency during this period, acting

⁶ It will be seen in subsequent figures that each of the terms contributes both positively and negatively to the N^2 tendency within the analysis domain. Thus, taking an average over the domain tends to wash out the positive and negative contributions. To circumvent this problem, the absolute value of each of the terms is averaged.

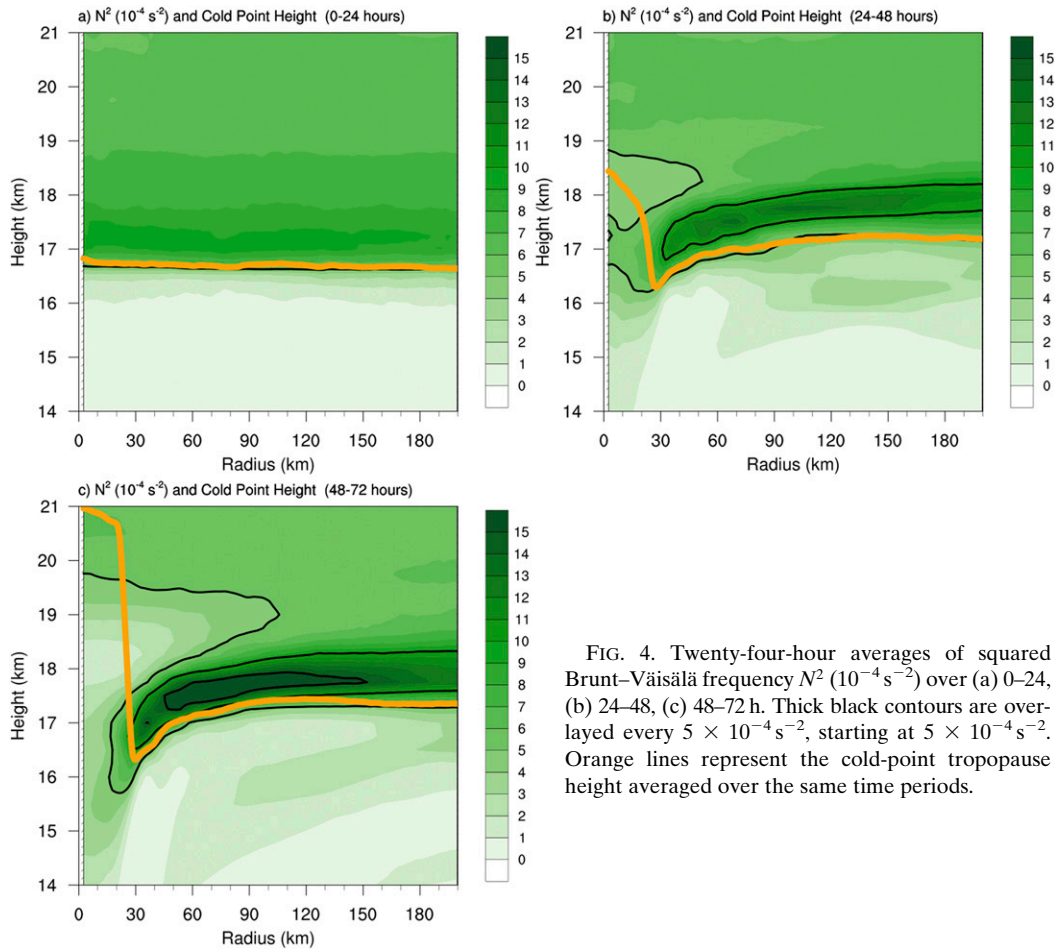


FIG. 4. Twenty-four-hour averages of squared Brunt–Väisälä frequency N^2 (10^{-4} s^{-2}) over (a) 0–24, (b) 24–48, (c) 48–72 h. Thick black contours are overlaid every $5 \times 10^{-4} \text{ s}^{-2}$, starting at $5 \times 10^{-4} \text{ s}^{-2}$. Orange lines represent the cold-point tropopause height averaged over the same time periods.

to stabilize near and just below the tropopause and destabilize above. Although vertical turbulence acted in opposition to advection (i.e., it acted to stabilize regions that advection acted to destabilize), the magnitude of the advective tendencies was larger, particularly at the innermost radii. The sum of advection and vertical turbulence (Fig. 5e) almost exactly replicated the static stability tendencies above the tropopause. Radiative tendencies, meanwhile (Fig. 5d), acted to destabilize the layer below about 16 km and stabilize the layer between 16 and 17 km. The sum of advection, vertical turbulence, and radiation (Fig. 5f) reproduced the total change in N^2 almost exactly.

2) 24–48 H

During the RI period, the maximum wind speed increased from 22 to 80 m s^{-1} (Fig. 1a). Over this time, N^2 within the eye generally decreased above 16 km and increased below (Fig. 6a), with the destabilization above 16 km maximizing near the level of the mean cold-point tropopause. These tendencies at the innermost radii

were driven almost entirely by advection (Fig. 6b). Vertical turbulence (Fig. 6c) and radiation (Fig. 6d) contributed negligibly to the static stability tendencies in this region.

Outside of the eye, the N^2 evolution exhibited alternating layers of positive and negative tendencies. Near and above 18 km existed an outward-sloping region of decreasing N^2 that extended out to the 180-km radius. In this region, neither vertical turbulence nor radiation exhibited negative N^2 tendencies; advection was the only forcing for this destabilization. Immediately below this layer, just above the cold-point tropopause, was a region of increasing N^2 that sloped outward from 17 km near the 30-km radius to just below 18 km outside of the 100-km radius. Both advection and vertical turbulence contributed to this positive N^2 tendency, with advection playing an important role below about 17.5 km and turbulence acting to stabilize the layer above 17.5 km. The sum of advection and turbulence (Fig. 6e) reveals two separate regions of increasing N^2 in the 17–18-km layer rather than one

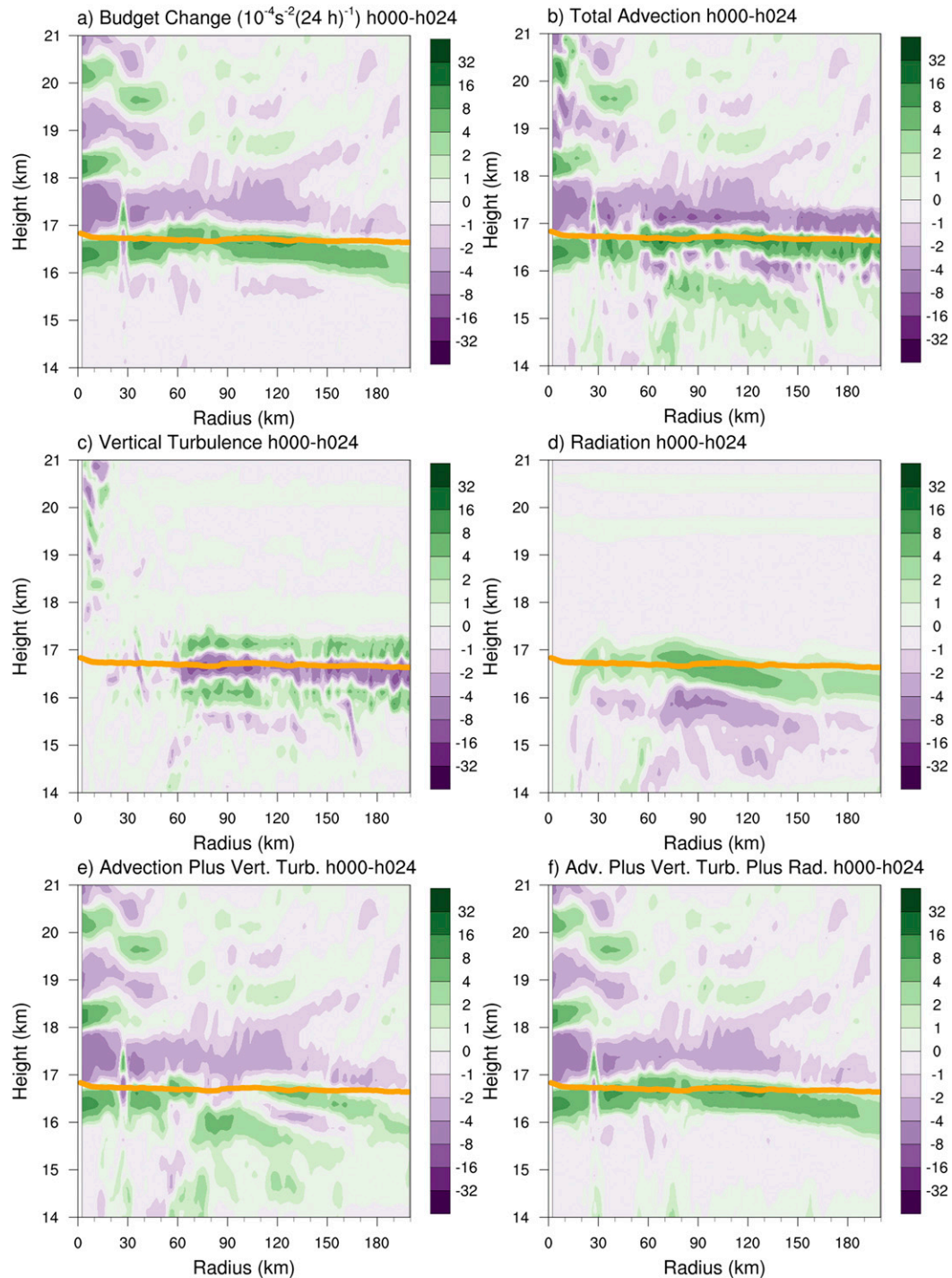


FIG. 5. (a) Total change in N^2 over the 0–24-h period [$10^{-4} \text{s}^{-2} (24 \text{ h})^{-1}$] and the contributions to that change from (b) the sum of horizontal and vertical advection, (c) vertical turbulence, (d) longwave and shortwave radiation, (e) the sum of horizontal advection, vertical advection, and vertical turbulence, and (f) the sum of horizontal advection, vertical advection, vertical turbulence, and longwave and shortwave radiation. Green shading indicates regions of stabilization and purple shading indicates regions of destabilization. Orange lines represent the cold-point tropopause height averaged over the 0–24-h period.

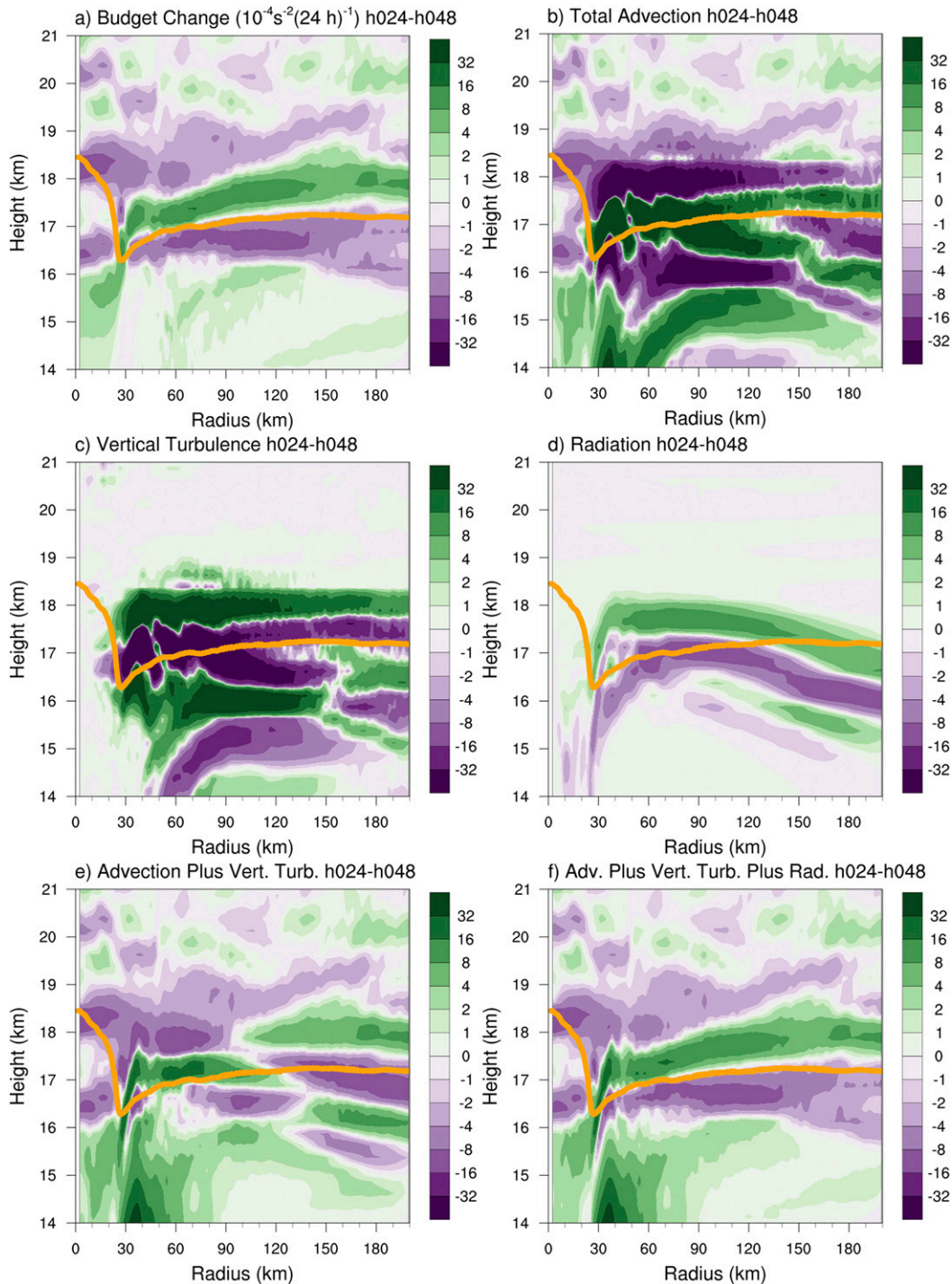


FIG. 6. As in Fig. 5, but for the 24–48-h period.

contiguous region. The addition of radiation to these two terms, however (Fig. 6f), provides the link between these two regions, indicating that radiation also plays a role in strengthening the stable layer just above the tropopause. In the 16–17-km layer, just below the cold-point

tropopause, a horizontally extensive layer of destabilization also was forced by a combination of advection, vertical turbulence, and radiation. The sum of advection and vertical turbulence accounts for only a portion of the decreasing N^2 in this layer, and actually

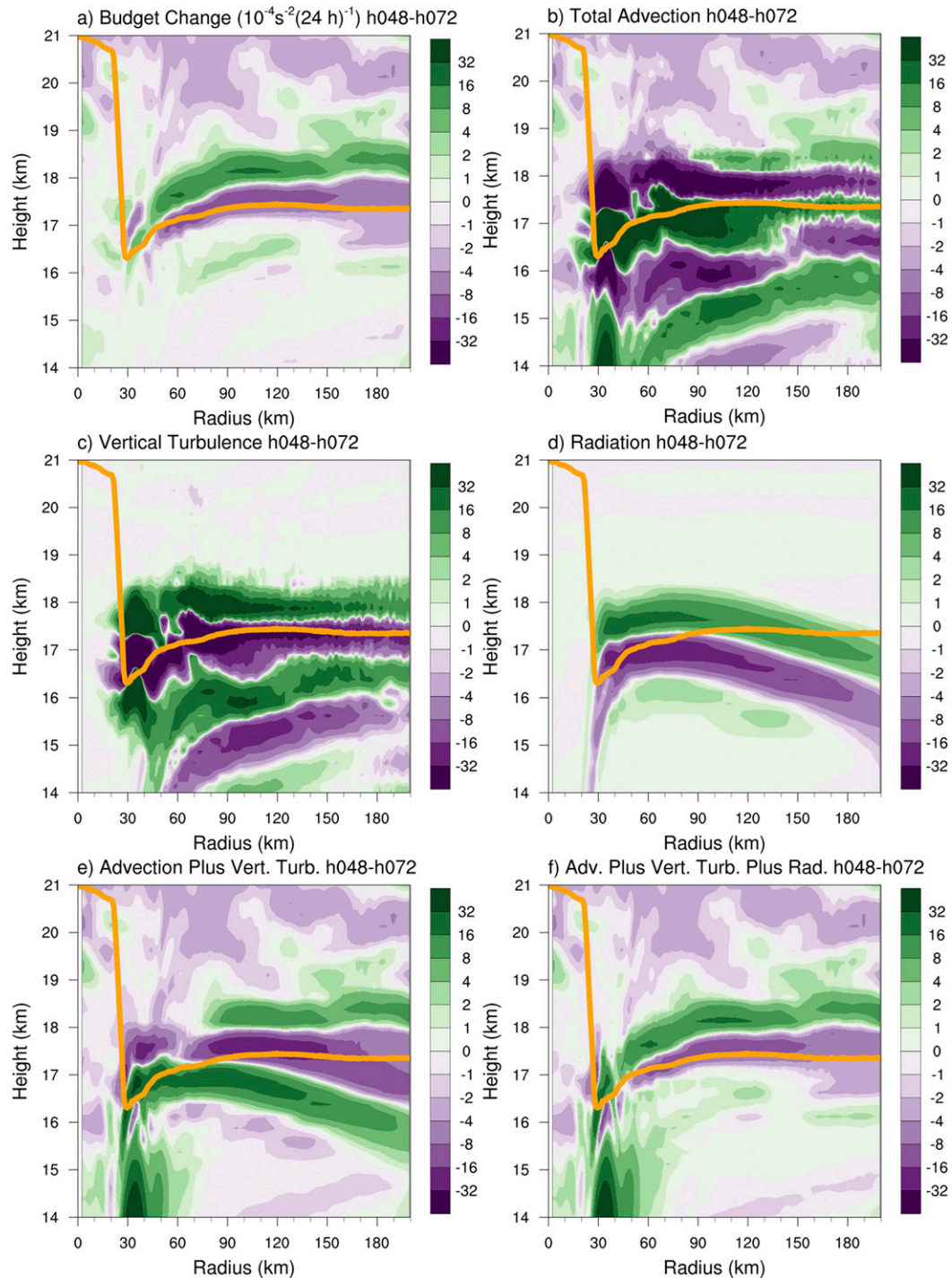


FIG. 7. As in Fig. 5, but for the 48–72-h period.

indicates forcing for stabilization near the 50-km radius and outside of the 130-km radius. Radiative tendencies overcome this forcing for stabilization in both of these regions to produce the radially extensive region of destabilization just below the tropopause. The sum of

advection, vertical turbulence, and radiation (Fig. 6f) once again closely follows the total N^2 variability, except in the 25–70-km radial band, where the neglect of latent heating and horizontal turbulence introduces some differences.

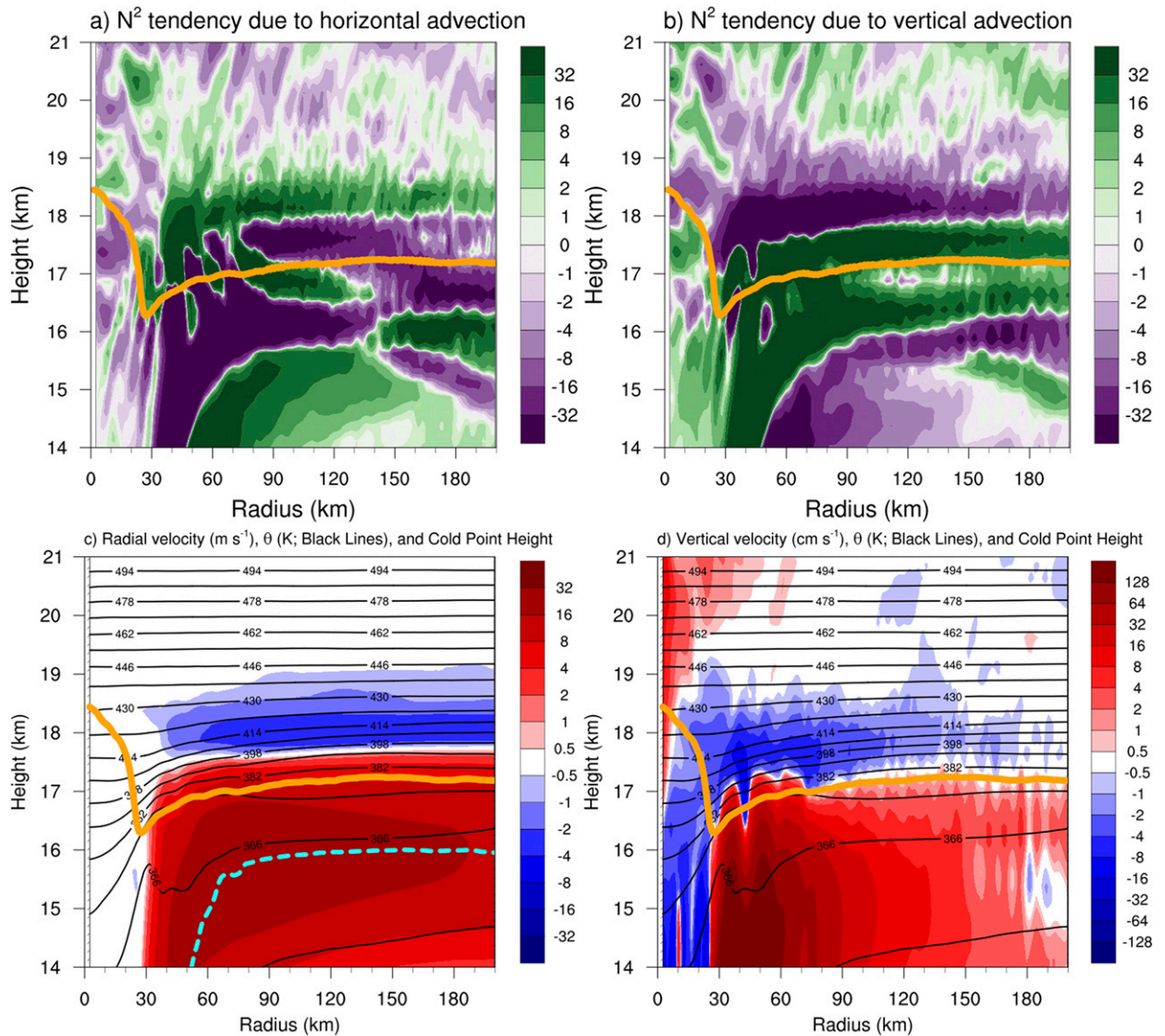


FIG. 8. The contributions to the change in N^2 over the 24–48-h period [$10^{-4} \text{ s}^{-2} (24 \text{ h})^{-1}$] by (a) the horizontal advection term and (b) the vertical advection term. (c) The radial velocity (m s^{-1} ; filled contours), potential temperature (K; thick black contours), cold-point tropopause height (orange line), and level of maximum outflow (dashed cyan line) averaged over the 24–48-h period. (d) The vertical velocity (cm s^{-1} ; filled contours), potential temperature (K; thick black contours), and cold-point tropopause height (orange line) averaged over the 24–48-h period.

3) 48–72 H

After the storm’s maximum wind speed leveled off near 80 m s^{-1} (Fig. 1a), the magnitude of the static stability tendencies within the eye decreased to near zero (Fig. 7a). Outside of the eye, however, N^2 continued to decrease in the layer immediately surrounding the tropopause and increase just above. The sum of advection and vertical turbulence (Fig. 7e) indicates that these two processes account for most of the destabilization near the tropopause and some of the stabilization near

the 18-km altitude. Below the tropopause, however, these two terms provided strong forcing for stabilization that did not manifest in the budget change (Fig. 7a). Radiation (Fig. 7d), which generally forced stabilization above 17 km and destabilization below, balanced out this forcing for stabilization in the upper troposphere. Within the 30–80-km radial band, advection and vertical turbulence combined to force destabilization in the 17–18-km layer (Fig. 7e), which did not manifest in the budget change (Fig. 7a). Radiation provided strong forcing for stabilization, which outweighed this effect

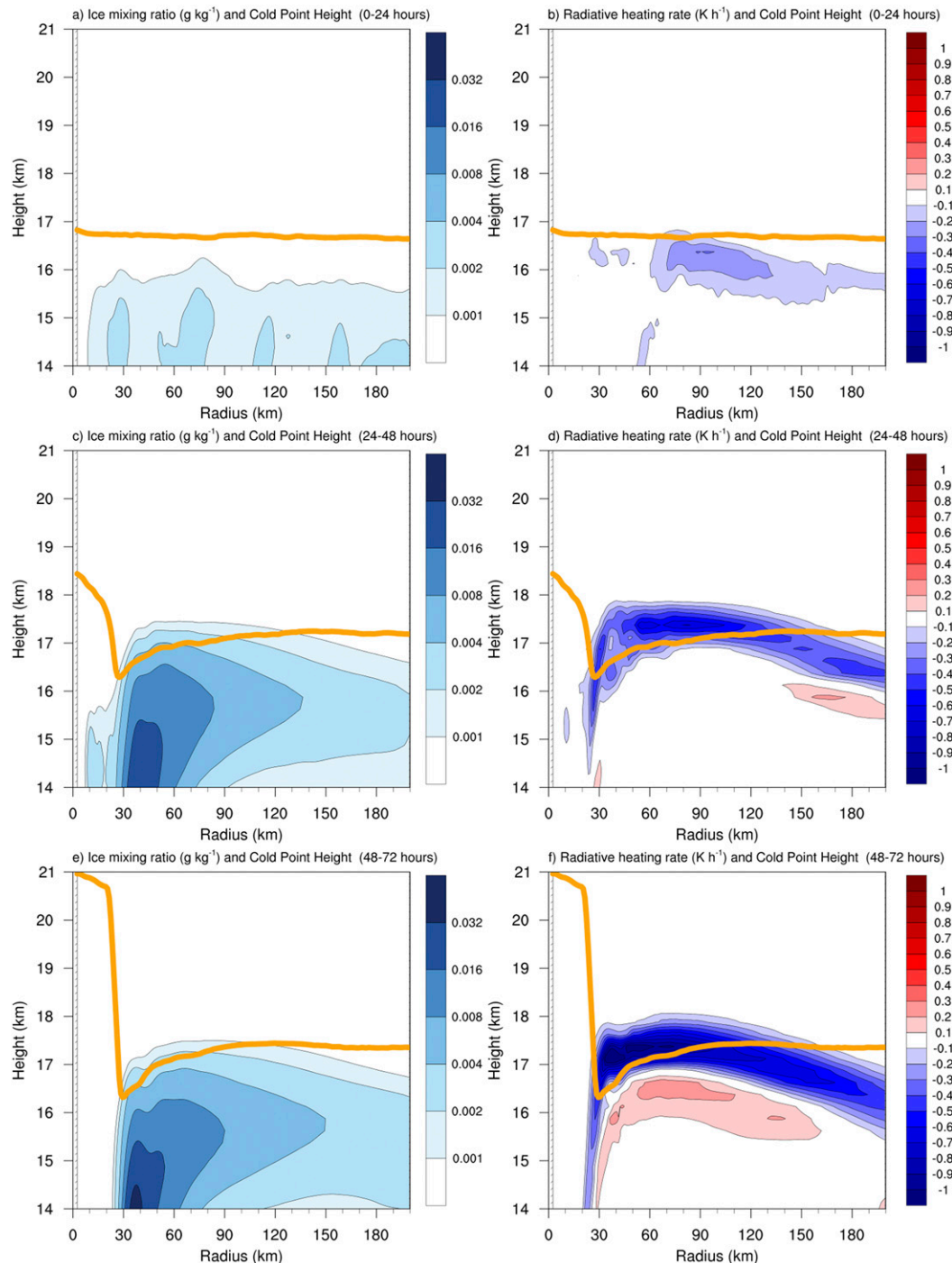


FIG. 9. (left) Ice mixing ratio (g kg^{-1}) and cold-point tropopause height (orange lines) averaged over (a) 0–24, (c) 24–48, and (e) 48–72 h. (right) Radiative heating rate (K h^{-1}) and cold-point tropopause height (orange lines) averaged over (b) 0–24, (d) 24–48, and (f) 48–72 h.

and produced net stabilization in a portion of this region. Outside of the 80-km radius, both advection (Fig. 7b) and vertical turbulence (Fig. 7c) provided forcing for stabilization near and just above the 18-km level.

The sum of the two terms (Fig. 7e) indicates increasing N^2 near the 18-km level everywhere outside of the 80-km radius, but this stabilization is slightly weaker in the 90–120-km radial band than the total budget tendency.

The addition of radiation (Fig. 7f) provided the extra forcing for stabilization required to account for the total increase in N^2 . Outside of the 120-km radius, the region of radiative forcing for stabilization sloped downward, and the increase in N^2 that appeared near 18 km can be explained entirely by a combination of advection and vertical turbulence.

5. Discussion

a. The role of the advection terms

Advection played an essential role in the tropopause-layer N^2 evolution at all stages of intensification, but for brevity, this section will focus only on the RI (24–48 h) period. To investigate the advective processes more closely, the individual contributions of horizontal and vertical advection during the RI period are shown in Fig. 8, along with the corresponding time-mean radial and vertical velocities and θ . The N^2 tendencies resulting from the two advective components (Figs. 8a,b) exhibited strong cancellation, consistent with flow that was nearly isentropic. There existed, however, a large region near the tropopause in which the total advective tendency was nonzero (Fig. 6b). These nonzero tendencies, which were partially canceled by turbulence tendencies, were related to the development of the TC’s secondary circulation as the storm intensified.

During the RI period, strong radial and vertical circulations developed near the tropopause (Figs. 8c,d), which forced high-magnitude N^2 tendencies caused by advection (Figs. 8a,b). A layer of strong outflow formed at and below the tropopause during this period, with the outflow maximum (dashed cyan line) curving from the 14-km level at the 50-km radius to just below the 16-km level outside of the 80-km radius (Fig. 8c). Notably, the N^2 tendency caused by horizontal advection (Fig. 8a) tended to switch signs at this line, with stabilization below the outflow maximum and destabilization above. Outside of the eye and eyewall, isentropes generally sloped upward with radius (Fig. 8c, black lines). Vertical wind shear acting on these upward-sloping isentropes should act to tilt them into the vertical above the outflow maximum, thereby decreasing $\partial\theta/\partial z$, and tilt them to be more horizontal below the outflow maximum, thereby increasing $\partial\theta/\partial z$. This mechanism is the same as that discussed in Trier and Sharman (2009), in which vertical wind shear in the outflow layer of a mesoscale convective system modified the upper-tropospheric static stability through differential advection of isentropes. Thus, wherever $\partial u/\partial z > 0$, the tilting term must force an increase in N^2 , and wherever $\partial u/\partial z < 0$, the tilting term must force a decrease in N^2 , which is the structure seen in Fig. 8a.

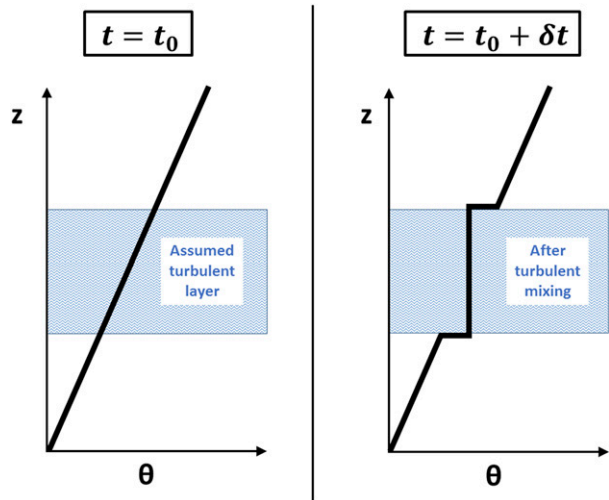


FIG. 10. Schematic diagram of the effect of turbulent mixing on the vertical profile of potential temperature θ . (left) At the initial time, potential temperature is assumed to increase with height at a constant rate (thick black line). The imposition of turbulence within a portion of the layer (blue hatching) adjusts the potential temperature profile toward the mean initial value of that layer. (right) After a period of mixing, the potential temperature in the mixed layer does not vary with height, but just above and just below the mixed layer, it rapidly increases with height.

Direct advection of N^2 by the radial wind [first term on the right-hand side of Eq. (6)] also acted within the outflow jet. For example, horizontal advection provided forcing for destabilization at the 16-km level almost everywhere inside of the 140-km radius. Outside of this radius near 16 km, however, existed a region of forcing for stabilization. This switch in signs can be explained by a reversal of the radial gradient of mean N^2 near the 140-km radius (Fig. 4b). Inside of that radius, $(\partial/\partial r)(\partial\theta/\partial z) > 0$ and $u > 0$, which corresponds to forcing for destabilization in Eq. (6); outside of that radius, $(\partial/\partial r)(\partial\theta/\partial z) < 0$ and $u > 0$, which corresponds to forcing for stabilization. The relative importance of the first and third terms on the right-hand side of Eq. (6) is difficult to ascertain, but the structure of the mean radial velocity, θ , and N^2 fields suggests that both terms are contributing within the outflow layer.

Meanwhile in the lower stratosphere, a thin layer of $2\text{--}4\text{ m s}^{-1}$ inflow developed about 1 km above the tropopause, similar to that which was observed in Hurricane Patricia (2015; Duran and Molinari 2018) and in previous modeling studies (e.g., Ohno and Satoh 2015; Kieu et al. 2016). Since the isentropes in this layer sloped slightly upward with radius (i.e., $\partial\theta/\partial r < 0$), this inflow acted to import lower- θ air from outer radii to inner radii. Since the negative θ tendencies maximized at the level of

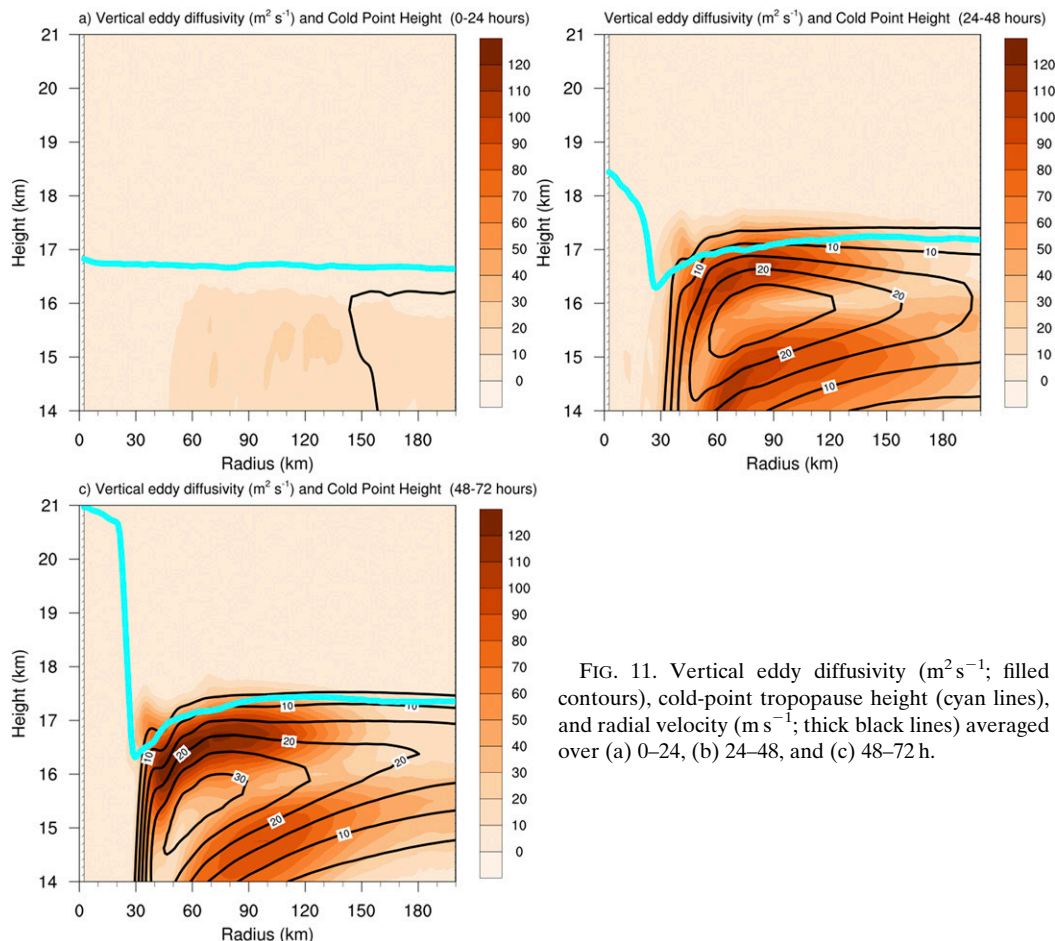


FIG. 11. Vertical eddy diffusivity ($\text{m}^2 \text{s}^{-1}$; filled contours), cold-point tropopause height (cyan lines), and radial velocity (m s^{-1} ; thick black lines) averaged over (a) 0–24, (b) 24–48, and (c) 48–72 h.

maximum inflow, radial advection provided forcing for destabilization below the inflow maximum and stabilization above (Fig. 8a).

Curiously, horizontal advection contributed to the N^2 tendency everywhere within the eye, even though the mean radial velocity there was near zero. Close examination of the model output revealed that these tendencies were forced by advective processes associated with inward-propagating waves. Although the radial velocity perturbations induced by these waves averaged out to zero, the advective tendencies forced by the radial velocity perturbations did not. Additionally, when these waves reached $r = 0$, a dipole of vertical velocity resulted, with ascent above and descent below. For reasons that remain unclear, the regions of ascent were more persistent than the regions of descent in the lower stratosphere, which resulted in the mean ascent that manifested near $r = 0$ above 17 km in Fig. 8d. The dynamics that force this mean stratospheric ascent near $r = 0$, and its potential consequences, are left for future work.

Vertical advection also played an important role in the tropopause-layer static stability evolution. Although the magnitude of the subsidence was larger at lower altitudes (below 15 km), $\partial\theta/\partial z$ was smaller there. Because $\partial\theta/\partial z$ was smaller, the subsidence at lower levels could not accomplish as much warming as the subsidence at higher levels in the eye, consistent with the results of Stern and Zhang (2013). As a result, vertical advection within the eye stabilized the layer below 16 km during RI.

Outside of the 27-km radius, ascent dominated the troposphere, while a 1–1.5-km-deep layer of descent existed immediately above the tropopause. These regions of ascent and descent converged just above the tropopause; this convergence acted to compact the isentropes in this layer and increase the static stability. Above the lower-stratospheric subsidence maximum, meanwhile, vertical advection decreased N^2 . Below the tropopause, differential vertical advection increased N^2 within the eyewall region, where upward vertical velocity decreased rapidly with height. Outside of the

eyewall below 16 km, meanwhile, the vertical gradient of vertical velocity was smaller, and as a result the N^2 tendencies caused by vertical advection were weaker.

Comparing the N^2 tendencies forced by horizontal (Fig. 8a) and vertical (Fig. 8b) advection to the total advective tendency seen in Fig. 6b reveals that horizontal advective tendencies dominated the troposphere, while vertical advective tendencies dominated the layer near and above the tropopause. Thus, tilting of isentropes in the vicinity of the upper-tropospheric outflow maximum appears to be the most important advective process governing the N^2 tendency in the troposphere, whereas convergence of vertical velocity dominates near the tropopause.

b. The role of radiation

During the initial spinup period (0–24 h; Fig. 9a), convection was not deep enough to deposit large quantities of ice near the tropopause and create a persistent cirrus canopy. Because of the lack of ice particles, the radiative heating tendencies during this period (Fig. 9b) were relatively small and confined to the region above a few particularly strong, although transient, convective towers. During RI (24–48 h), the eyewall updraft strengthened and a radially extensive cirrus canopy developed near the tropopause (Fig. 9c). The enhanced vertical gradient of ice mixing ratio at the top of the cirrus canopy induced strong diurnal-mean radiative cooling near the tropopause (Fig. 9d). This cooling exceeded 0.6 K h^{-1} (14.4 K day^{-1}) in some places and sloped downward from the lower stratosphere into the upper troposphere, following the top of the cirrus canopy. A small radiative warming maximum also appeared outside of the 140-km radius below this region of cooling. These results broadly agree with those of Bu et al. (2014, see their Fig. 11a), whose CM1 simulations produced a 0.3 K h^{-1} diurnally averaged radiative cooling at the top of the cirrus canopy and radiative warming within the cloud that maximized near the 200-km radius. This broad region of radiative cooling acted to destabilize the layer below the cooling maximum and to stabilize the layer above, which can be seen in Fig. 6d. The small area of net radiative heating outside of the 140-km radius enhanced the destabilization above 16 km in this region and produced a thin layer of stabilization in the 15–16-km layer.

After the TC’s RI period completed (48–72 h), strong radiative cooling remained near the tropopause at inner radii (Fig. 9f), sloping downward with the top of the cirrus canopy to below the tropopause at outer radii. Cooling rates exceeded 1 K h^{-1} (24 K day^{-1}) just above the tropopause between the 30- and 70-km radii. This value is more than 3 times the maximum cooling

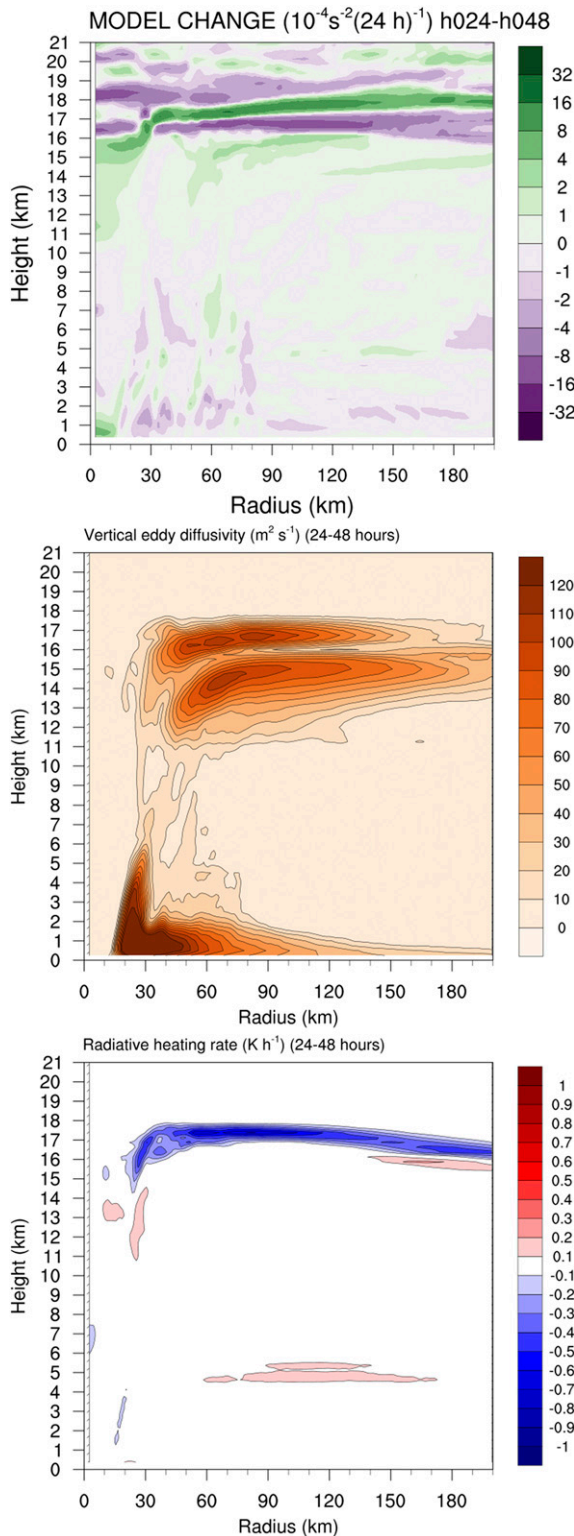


FIG. 12. (top) Change in N^2 over the 24–48-h period [$10^{-4} \text{ s}^{-2} (24 \text{ h})^{-1}$] directly output by the model for the 0–21-km layer. (middle) Vertical eddy diffusivity ($\text{m}^2 \text{ s}^{-1}$) averaged over the same time period. (bottom) Radiative heating rate (K h^{-1}) averaged over the same time period.

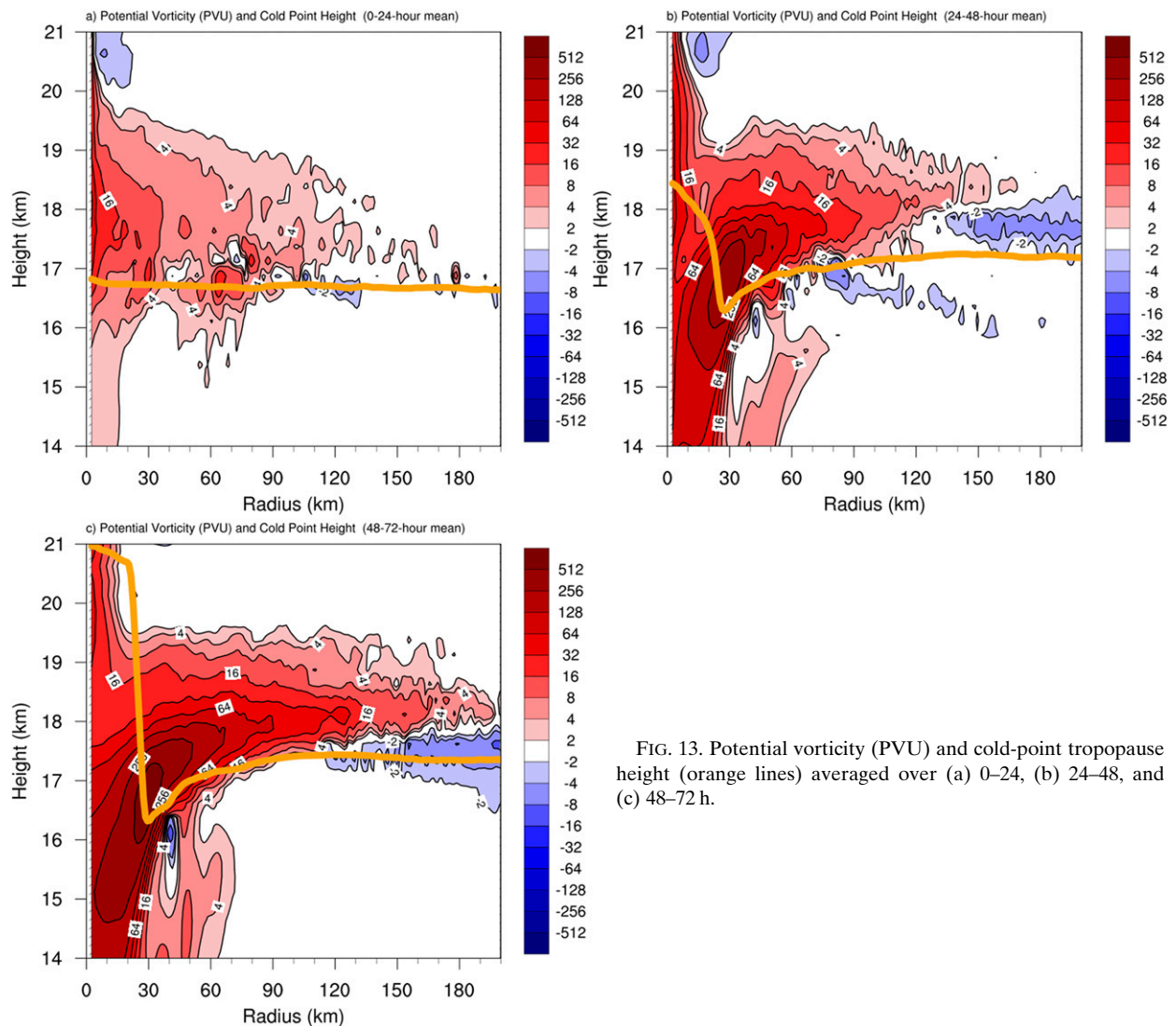


FIG. 13. Potential vorticity (PVU) and cold-point tropopause height (orange lines) averaged over (a) 0–24, (b) 24–48, and (c) 48–72 h.

rate of 0.3 K h^{-1} noted by Bu et al. (2014), a difference that is a consequence of their larger vertical grid spacing compared to that used here, along with a contribution from differing radiation schemes. To compare our results to theirs, we ran a simulation identical to that described in section 2, except using the NASA Goddard radiation scheme and 625-m vertical grid spacing, to match those of Bu et al. (2014). This simulation produced a maximum 24-h-average radiative cooling rate of 0.3 K h^{-1} (not shown), which agrees with that shown in Bu et al. (2014). Another simulation using 625-m vertical grid spacing and RRTMG radiation produced 24-h-average cooling rates of up to 0.6 K h^{-1} . This suggests that vertical grid spacing smaller than 625 m is necessary to resolve properly the radiative cooling at the top of the cirrus canopy, and

that the results can be quite sensitive to the radiation scheme used. A more in-depth analysis of this sensitivity to vertical grid spacing and radiation scheme is left to future work; it is possible that a vertical grid spacing even smaller than 250 m is necessary to resolve cloud-top radiative tendencies.

Meanwhile below the tropopause, time-mean radiative warming was present between the 30- and 160-km radii within the cirrus canopy. The existence of radiative cooling overlying radiative warming in this region led to radiatively forced destabilization at and below the tropopause, as was depicted in Fig. 7d. Beneath the warming layer existed a region of forcing for stabilization, while a much stronger region of forcing for stabilization existed in the lower stratosphere, above the cooling maximum.

The results herein suggest that after the cirrus canopy developed, radiative heating tendencies considerably destabilized the upper troposphere and stabilized the lower stratosphere at inner radii. At larger radii, the downward slope of these tendencies with radius produced a region of radiative forcing for stabilization just below the tropopause. The departure of the cirrus canopy from the tropopause at these large radii (Figs. 9c,e) suggests that in this region, the tropopause did not exert a strong control on the height of the cirrus canopy. Other processes, such as the precipitation of ice particles, must have caused this lowering of the cloud top. The effect of the interaction of radiation with clouds near the tropopause is further investigated in the appendix.

c. The role of turbulent mixing

Figure 10 depicts the effect of turbulent mixing on the vertical θ profile of an initially stably stratified layer. At the initial time in this schematic, θ is assumed to increase with height at a constant rate (Fig. 10, left panel). The imposition of turbulence (blue hatching) adjusts the θ profile within the mixed layer toward a constant value equal to the mean value of that layer in the initial state (Fig. 10, right panel). Just above and just below the mixed layer, however, the θ profile remains undisturbed. Consequently, although turbulent mixing acts to decrease $\partial\theta/\partial z$ in the layer in which it is occurring, it actually increases $\partial\theta/\partial z$ just below and just above the layer. Vertical gradients of turbulent mixing like those depicted here are quite important, particularly on the flanks of the upper-tropospheric outflow jet.

Two distinct maxima of vertical eddy diffusivity developed in the tropopause layer as the storm intensified (Fig. 11). A comparison of these turbulent regions to the N^2 tendencies in Figs. 6c and 7c reveals that layers characterized by large vertical gradients of vertical eddy diffusivity corresponded to layers of destabilization caused by vertical turbulence. Just outside of these layers, however, vertical turbulence acted to increase N^2 . The large vertical gradient of vertical eddy diffusivity near the tropopause contributed to the development of the lower-stratospheric stable layer during RI. These results support the hypothesized role of turbulence in setting the outflow-layer θ stratification in Emanuel and Rotunno (2011), although more experiments with different turbulence parameterizations are needed to investigate this problem more closely.

6. Conclusions and future work

The simulated N^2 evolution shown herein closely resembled that observed during the RI of Hurricane Patricia (2015). Three N^2 budget terms dominated in the

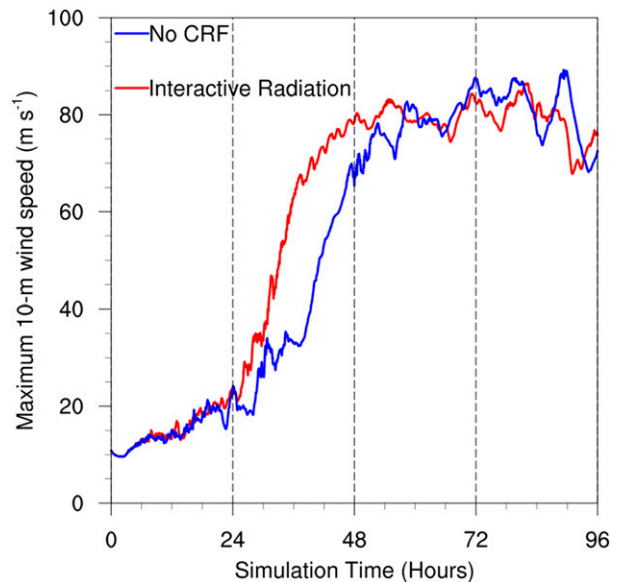


FIG. A1. Maximum 10-m wind speed (m s^{-1}) for the simulation described in section 2 (red), and an identical simulation except radiation is not permitted to interact with condensate (blue).

upper troposphere and lower stratosphere: advection, radiation, and vertical turbulence. Advection dominated within the eye, where it provided forcing for lower-stratospheric destabilization. Meanwhile, radiation and vertical turbulence greatly contributed to developing the strong N^2 maximum just above the cold-point tropopause during RI.

To put the N^2 variability seen near the tropopause into context, Fig. 12 depicts the model change in N^2 over the RI period (hours 24–48) from 0- to 21-km altitude, along with the vertical eddy diffusivity and the radiative heating rate. The largest changes in N^2 occurred in a relatively shallow layer immediately surrounding the tropopause (Fig. 12a). This shallow layer also contained the largest diurnally averaged radiative heating tendencies found anywhere in the domain (Fig. 12c). Values of vertical eddy diffusivity larger than any found outside of the boundary layer also resided in the upper troposphere (Fig. 12b). The results herein suggest that this turbulence not only developed as a response to the presence of small static stability and large vertical wind shear, as discussed by Molinari et al. (2014) and Duran and Molinari (2016), but also can actively increase the static stability in highly localized regions just above and below the mixed layers.

Since two of the most important processes contributing to the N^2 variability are parameterized, and one (radiation) closely depends on yet another parameterized process (microphysics), the tropopause-layer N^2 variability could be quite sensitive to the assumptions

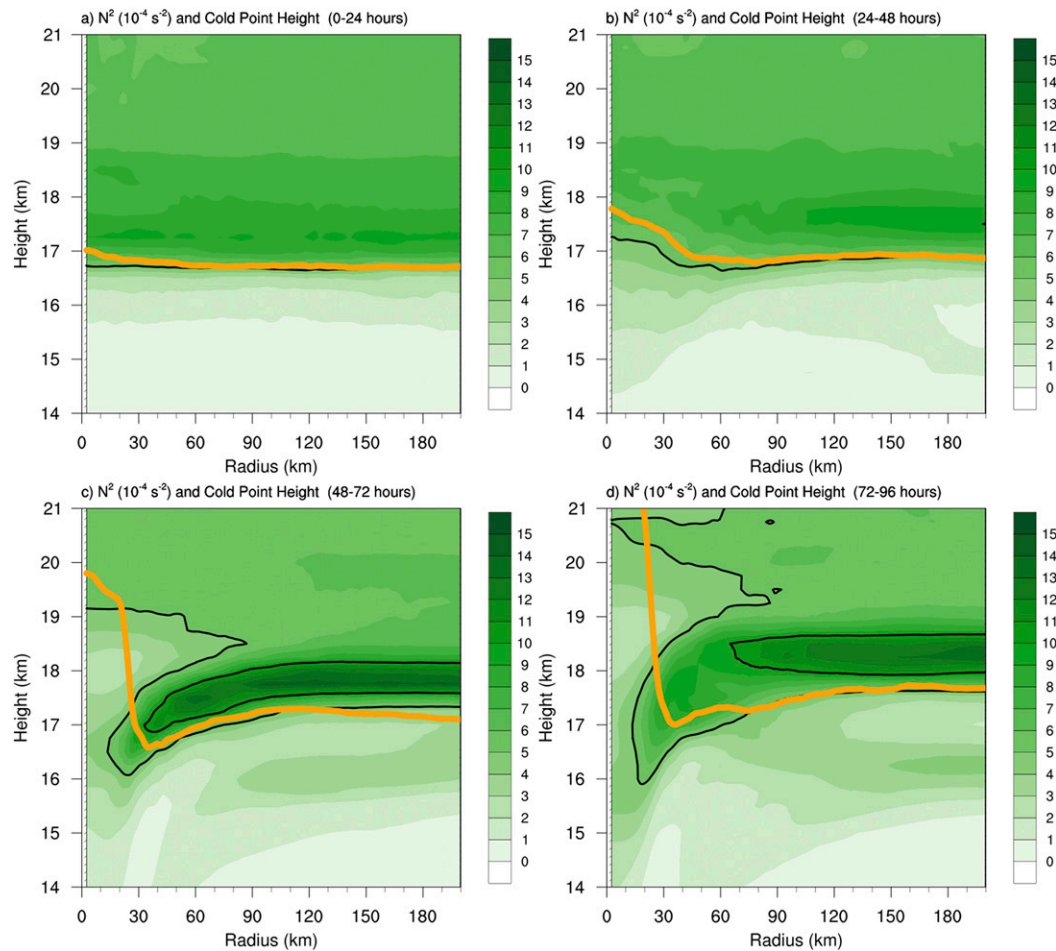


FIG. A2. As in Fig. 4, but for the simulation in which radiation is not permitted to interact with condensate.

inherent to the parameterizations used. A better understanding of the microphysical characteristics of the TC cirrus canopy, its interaction with radiation, and outflow-layer turbulence is critical to understanding the tropopause-layer N^2 evolution.

An interesting consequence of increasing N^2 in the tropopause layer is its effect on potential vorticity (PV) near the tropopause. As the simulated TC intensified, PV increased considerably inside of the eye as relative vorticity strengthened within the radius of maximum winds (Fig. 13). Outside of the eye in the lower stratosphere, meanwhile, PV also increased as a consequence of strengthening static stability. The magnitude of PV in this layer is exceptionally large, but it is consistent with analyses produced using observations from Hurricane Patricia (2015) that showed values exceeding 200 PVU ($1 \text{ PVU} = 10^{-6} \text{ K kg}^{-1} \text{ m}^2 \text{ s}^{-1}$) near the tropopause (Bell et al. 2018). Just above and below the tropopause at larger radii, meanwhile, negative PV developed as a consequence of strong anticyclonic relative vorticity

associated with the TC outflow layer. An investigation of the details and consequences of this tropopause-layer PV evolution are left to future work, but these results suggest that the static stability tendency near the tropopause is an important consideration in such an analysis.

In this paper all of the variables were averaged over a full diurnal cycle to eliminate the effects of diurnal variability and to isolate the overall storm evolution. A preliminary investigation of the diurnal cycle of N^2 using an ensemble of CM1 simulations suggests that the static stability at the top of the cirrus canopy peaks in the early afternoon and decreases overnight (S. Ditchek 2018, personal communication). The mechanisms that produce this diurnal cycle of static stability, and its potential consequences, are the subject of future work.

Acknowledgments. This work constituted a portion of the lead author's Ph.D. dissertation, which benefited from the guidance of committee members Kristen

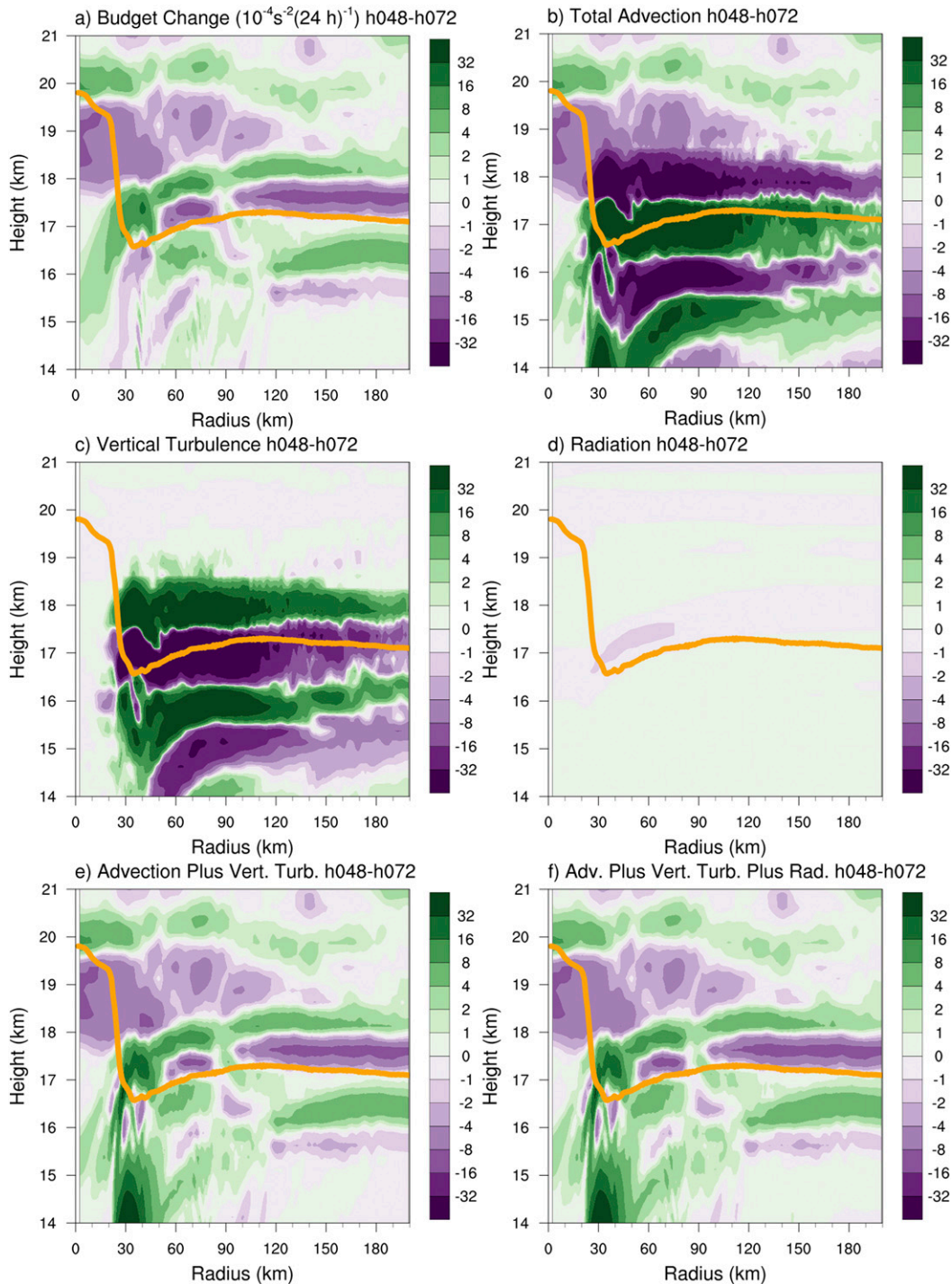


FIG. A3. As in Fig. 7, but for the simulation in which radiation is not permitted to interact with condensate.

Corbosiero, Robert Fovell, Brian Tang, and Ryan Torn. We thank George Bryan for his continued development and support of Cloud Model 1, and Jeffrey Kepert and Erika Duran for the helpful conversations related to this work. Comments from Kerry Emanuel and two

anonymous reviewers improved a previous version of this manuscript. This research was supported by NSF Grant AGS-1636799 and Office of Naval Research Grant N000141712110 as a part of the TCI Departmental Research Initiative.

APPENDIX

Sensitivity to Cloud-Radiative Forcing

To analyze more closely the effect of cloud-radiative forcing on the N^2 evolution, a simulation identical to that described in section 2 was run, except the interaction between condensate and radiation was prohibited [as was described in Bu et al. (2014) and Fovell et al. (2016)]. The intensity evolution of this simulation (Fig. A1, blue line) compares well with that of the simulation described in section 2 (Fig. A1, red line), except the storm without cloud-radiative forcing took longer to begin its RI period. The 24-h averages of N^2 reveal a similar overall evolution in the two simulations (cf. Figs. 4 and A2), except the lower-stratospheric N^2 maximum does not become as strong in the simulation without cloud-radiative forcing. The magnitude of the sum of the advection and turbulence terms immediately surrounding the tropopause in this simulation (Fig. A3e) is not as large as that in the full-radiation simulation (Fig. 7e). This suggests that radiative heating tendencies near the cloud top affect the radial-vertical circulation there, which then feeds back onto the advection and turbulence terms. The smaller turbulence and advective tendencies, combined with the near-zero radiative heating tendencies (Fig. A3d), lead to a smaller lower-stratospheric stabilization tendency (cf. Figs. 7a and A3a). These results highlight the importance of cloud-radiative interaction in the evolution of the tropopause-layer N^2 .

REFERENCES

- Bell, M. M., J. Martinez, J. D. Doyle, and R. F. Rogers, 2018: Potential vorticity structure and evolution of Hurricane Patricia (2015). *33rd Conf. on Hurricanes and Tropical Meteorology*, Ponte Vedra, FL, Amer. Meteor. Soc., 12B.3, <https://ams.confex.com/ams/33HURRICANE/webprogram/Paper340245.html>.
- Bowman, K. P., and M. D. Fowler, 2015: The diurnal cycle of precipitation in tropical cyclones. *J. Climate*, **28**, 5325–5334, <https://doi.org/10.1175/JCLI-D-14-00804.1>.
- Bryan, G. H., 2017: The governing equations for CM1. UCAR Publ. 24 pp., http://www2.mmm.ucar.edu/people/bryan/cm1/cm1_equations.pdf.
- , and R. Rotunno, 2009: The maximum intensity of tropical cyclones in axisymmetric numerical model simulations. *Mon. Wea. Rev.*, **137**, 1770–1789, <https://doi.org/10.1175/2008MWR2709.1>.
- Bu, Y. P., R. G. Fovell, and K. L. Corbosiero, 2014: Influence of cloud-radiative forcing on tropical cyclone structure. *J. Atmos. Sci.*, **71**, 1644–1622, <https://doi.org/10.1175/JAS-D-13-0265.1>.
- Chen, H., and D.-L. Zhang, 2013: On the rapid intensification of Hurricane Wilma (2005). Part II: Convective bursts and the upper-level warm core. *J. Atmos. Sci.*, **70**, 146–162, <https://doi.org/10.1175/JAS-D-12-062.1>.
- , and S. G. Gopalakrishnan, 2015: A study of the asymmetric rapid intensification of Hurricane Earl (2010) using the HWRf system. *J. Atmos. Sci.*, **72**, 531–549, <https://doi.org/10.1175/JAS-D-14-0097.1>.
- Dinh, T. P., D. R. Durran, and T. P. Ackerman, 2010: Maintenance of tropical tropopause layer cirrus. *J. Geophys. Res.*, **115**, D02104, <https://doi.org/10.1029/2009JD012735>.
- Doyle, J. D., and Coauthors, 2017: A view of tropical cyclones from above: The Tropical Cyclone Intensity (TCI) Experiment. *Bull. Amer. Meteor. Soc.*, **98**, 2113–2134, <https://doi.org/10.1175/BAMS-D-16-0055.1>.
- Dunion, J. P., C. D. Thorncroft, and C. S. Velden, 2014: The tropical cyclone diurnal cycle of mature hurricanes. *Mon. Wea. Rev.*, **142**, 3900–3919, <https://doi.org/10.1175/MWR-D-13-00191.1>.
- Duran, P., and J. Molinari, 2016: Upper-tropospheric low Richardson number in tropical cyclones: Sensitivity to cyclone intensity and the diurnal cycle. *J. Atmos. Sci.*, **73**, 545–554, <https://doi.org/10.1175/JAS-D-15-0118.1>.
- , and —, 2018: Dramatic inner-core tropopause variability during the rapid intensification of Hurricane Patricia (2015). *Mon. Wea. Rev.*, **146**, 119–134, <https://doi.org/10.1175/MWR-D-17-0218.1>.
- Durran, D. R., T. Dinh, M. Ammerman, and T. Ackerman, 2009: The mesoscale dynamics of thin tropical tropopause cirrus. *J. Atmos. Sci.*, **66**, 2859–2873, <https://doi.org/10.1175/2009JAS03046.1>.
- Emanuel, K., 2012: Self-stratification of tropical cyclone outflow. Part II: Implications for storm intensification. *J. Atmos. Sci.*, **69**, 988–996, <https://doi.org/10.1175/JAS-D-11-0177.1>.
- , and R. Rotunno, 2011: Self-stratification of tropical cyclone outflow. Part I: Implications for storm structure. *J. Atmos. Sci.*, **68**, 2236–2249, <https://doi.org/10.1175/JAS-D-10-05024.1>.
- Fovell, R. G., Y. P. Bu, K. L. Corbosiero, W.-w. Tung, Y. Cao, H.-C. Kuo, L.-H. Hsu, and H. Su, 2016: Influence of cloud microphysics and radiation on tropical cyclone structure and motion. *Multiscale Convection-Coupled Systems in the Tropics: A Tribute to Dr. Michio Yanai, Meteor. Monogr.*, No. 56, Amer. Meteor. Soc., <https://doi.org/10.1175/AMSMONOGRAPHIS-D-15-0006.1>.
- Iacono, M. J., J. S. Delamere, E. J. Mlawer, M. W. Shephard, S. A. Clough, and W. D. Collins, 2008: Radiative forcing by long-lived greenhouse gases: Calculations with the AER radiative transfer models. *J. Geophys. Res.*, **113**, D13103, <https://doi.org/10.1029/2008JD009944>.
- Kepert, J. D., J. Schwendike, and H. Ramsay, 2016: Why is the tropical cyclone boundary layer not “well mixed”? *J. Atmos. Sci.*, **73**, 957–973, <https://doi.org/10.1175/JAS-D-15-0216.1>.
- Kieu, C., V. Tallapragada, D.-L. Zhang, and Z. Moon, 2016: On the development of double warm-core structures in intense tropical cyclones. *J. Atmos. Sci.*, **73**, 4487–4506, <https://doi.org/10.1175/JAS-D-16-0015.1>.
- Kimberlain, T. B., E. S. Blake, and J. P. Cangialosi, 2016: Tropical cyclone report: Hurricane Patricia. National Hurricane Center Rep. EP202015, 32 pp., https://www.nhc.noaa.gov/data/tcr/EP202015_Patricia.pdf.
- Komaromi, W. A., and J. D. Doyle, 2017: Tropical cyclone outflow and warm core structure as revealed by HS3 dropsonde data. *Mon. Wea. Rev.*, **145**, 1339–1359, <https://doi.org/10.1175/MWR-D-16-0172.1>.
- Kossin, J., 2002: Daily hurricane variability inferred from GOES infrared imagery. *Mon. Wea. Rev.*, **130**, 2260–2270, [https://doi.org/10.1175/1520-0493\(2002\)130<2260:DHVIFG>2.0.CO;2](https://doi.org/10.1175/1520-0493(2002)130<2260:DHVIFG>2.0.CO;2).
- Leppert, K. D., II, and D. J. Cecil, 2016: Tropical cyclone diurnal cycle as observed by TRMM. *Mon. Wea. Rev.*, **144**, 2793–2808, <https://doi.org/10.1175/MWR-D-15-0358.1>.

- Markowski, P. M., and G. H. Bryan, 2016: LES of laminar flow in the PBL: A potential problem for convective storm simulations. *Mon. Wea. Rev.*, **144**, 1841–1850, <https://doi.org/10.1175/MWR-D-15-0439.1>.
- Molinari, J., P. Duran, and D. Vollaro, 2014: Low Richardson number in the tropical cyclone outflow layer. *J. Atmos. Sci.*, **71**, 3164–3179, <https://doi.org/10.1175/JAS-D-14-0005.1>.
- Navarro, E. L., and G. J. Hakim, 2016: Idealized numerical modeling of the diurnal cycle of tropical cyclones. *J. Atmos. Sci.*, **73**, 4189–4201, <https://doi.org/10.1175/JAS-D-15-0349.1>.
- Ohno, T., and M. Satoh, 2015: On the warm core of a tropical cyclone formed near the tropopause. *J. Atmos. Sci.*, **72**, 551–571, <https://doi.org/10.1175/JAS-D-14-0078.1>.
- Rogers, R. F., S. Aberson, M. M. Bell, D. J. Cecil, J. D. Doyle, J. Morgerman, L. K. Shay, and C. Velden, 2017: Rewriting the tropical record books: The extraordinary intensification of Hurricane Patricia (2015). *Bull. Amer. Meteor. Soc.*, **98**, 2091–2112, <https://doi.org/10.1175/BAMS-D-16-0039.1>.
- Rotunno, R., and K. A. Emanuel, 1987: An air–sea interaction theory for tropical cyclones. Part II: Evolutionary study using a nonhydrostatic axisymmetric numerical model. *J. Atmos. Sci.*, **44**, 542–561, [https://doi.org/10.1175/1520-0469\(1987\)044<0542:AAITFT>2.0.CO;2](https://doi.org/10.1175/1520-0469(1987)044<0542:AAITFT>2.0.CO;2).
- Stern, D. P., and F. Zhang, 2013: How does the eye warm? Part I: A potential temperature budget analysis of an idealized tropical cyclone. *J. Atmos. Sci.*, **70**, 73–89, <https://doi.org/10.1175/JAS-D-11-0329.1>.
- Thompson, G., R. M. Rasmussen, and K. Manning, 2004: Explicit forecasts of winter precipitation using an improved bulk microphysics scheme. Part I: Description and sensitivity analysis. *Mon. Wea. Rev.*, **132**, 519–542, [https://doi.org/10.1175/1520-0493\(2004\)132<0519:EFOWPU>2.0.CO;2](https://doi.org/10.1175/1520-0493(2004)132<0519:EFOWPU>2.0.CO;2).
- Trier, S. B., and R. D. Sharman, 2009: Convection-permitting simulations of the environment supporting widespread turbulence within the upper-level outflow of a mesoscale convective system. *Mon. Wea. Rev.*, **137**, 1972–1990, <https://doi.org/10.1175/2008MWR2770.1>.